Supplementary Materials for

Organization of the Influenza Virus Replication Machinery

Arne Moeller*, Robert N. Kirchdoerfer*, Clinton S. Potter,
Bridget Carragher, Ian A. Wilson

correspondence to: bcarr@scripps.edu; wilson@scripps.edu

This PDF file includes:

Materials and Methods
Figs. S1 to S17
Table S1
Captions for Movies S1 to S3

Other Supplementary Materials for this manuscript includes the following:

Movies S1 to S3

Materials and Methods

Protein expression and purification

pHW193 carrying the PA subunit was modified to encode an N-terminal FLAG-TEV tag using MPIPE (*42*). The modified pHW193 along with pHW191, pHW192 and pHW195 that correspond to gene segments 3, 1, 2 and 5 (PA, PB2, PB1 and NP) from influenza A/Puerto Rico/8/1934 (H1N1) virus (*13*) were co-transfected into 80% confluent 293T17 cells (ATCC CRL-11268) with PEI-MAX (Polysciences). At 36 hours post-transfection, cells were washed in 50 mM Tris-Cl pH 7.9, 150 mM NaCl and lysed in 50 mM Tris-Cl pH 7.9, 300 mM NaCl, 5 mM $MgCl_2$, 10% glycerol, 0.05% Igepal CA-630, 2 mM DTT, 10 mM vanadyl ribonucleoside complexes (New England Biosciences) and Complete Protease Inhibitors without EDTA (Roche) at 4˚C for 15 minutes. The lysate was cleared by centrifugation and bound in batch to M2 FLAG resin (Sigma Aldrich) for 1 hour. Resin was collected and washed with 5 column volumes of additional lysis buffer without protease inhibitors or vanadyl ribonucleoside complexes and 15 column volumes of 50 mM Tris-Cl pH 7.9, 50 mM Na_2HPO_4, 200 mM NaCl, 2 mM DTT. Bound protein was eluted from the column in the same buffer with 100 µg/mL FLAG peptide. Elutions were immediately concentrated by ultrafiltration (Amicon Ultra 4, 100 kDa MWCO) and 1/20 volumes of ribonuclease inhibitor (SUPERASE-In, Ambion) were added to improve complex stability and integrity. A_{260}/A_{280} ratio for the complex was 1.6 similar to that observed for ribonucleoprotein complexes purified from influenza virions (*43*). For gold-label studies, the complexes were prepared as described above. Additionally, the pHW191 construct was modified to encode a C-terminal TEV-His_6 tag for binding of Ni-NTA 5 nm NanoGold (Nanoprobes).

Free polymerase was expressed as described above. Cells were lysed in 50 mM AMPD pH 8.5, 50 mM Li_2SO_4, 100 mM NaCl, 10% glycerol, 0.05% Igepal CA-630, 2 mM DTT, 25 µg/mL RNase A (Roche) and Complete Protease Inhibitors without EDTA (Roche) at 4˚C for 15 minutes. Lysates were cleared by centrifugation and filtration. M2 FLAG agarose was used to bind polymerase from the lysate. The resin was washed with lysis buffer followed by 50 mM AMPD pH 8.5, 50 mM Li_2SO_4, 100 mM NaCl, 0.01045% Brij-35, 2 mM DTT and eluted in the same buffer with 100 µg/mL FLAG peptide. The protein was further purified by heparin chromatography (Pall) using a 0.3-0.9 M NaCl step gradient. The final purification was done on a Superose 6 column (GE Life Sciences) using a buffer identical to the FLAG wash buffer. A_{260}/A_{280} ratio for the purified polymerase was 1.0 indicating that most, although not all, of the RNA had been removed during purification.

Specimen preparation and electron microscopy

Samples for negative stain were applied onto freshly glow discharged carbon coated copper grids. Sample was reduced to a thin film by blotting, and a 1% solution of uranyl formate negative stain was then immediately applied to the grid and blotted off from the same side. The negative stain process was repeated three times. For cryo-EM, samples were applied onto freshly plasma-cleaned (7 s, GATAN-SOLARUS) C-flat grids (2 µm hole) and flash frozen in liquid ethane using a Vitrobot (for RNPs) or a standard manual flash freezing device (for RNA polymerase).

Data were acquired using one of two Tecnai F20 Twin transmission electron microscopes operating at 120 kV. Images were automatically collected using the LEGINON system (*44*). Images were recorded using a Tietz or GATAN 4k x 4k pixel CCD camera.

Data processing

Experimental data were processed by the Appion software package (*45*). Specific information on number of micrographs, particle counts, etc. is provided in table S1. The defoci were estimated using ctffind3 (*46*)and ACE2 (*45*) and ctf correction was done by phase flipping the whole micrograph. Particles were selected manually or automatically depending on the sample (*47, 48*). After stack creation in APPION all datasets were prealigned and classified using 2-D maximum likelihood procedures and multivariate statistical analysis as implemented in XMIPP and IMAGIC (*15, 49, 50*). Resulting class averages were manually inspected and classes that represented noise or distorted particles were rejected.

Image analysis of influenza virus RNP

Random Conical Tilt (RCT) (*51*) reconstructions of the RNP central filament were generated from tilt pairs of negatively stained particles using APPION. This initial analysis was followed by further analysis of the RNP filaments preserved in vitreous ice. For initial model creation, several different strategies were used. For the RNP central filament region, the particles were considered as side views of filaments lying in a plane. Thus, after rotational alignment and classification, only one Euler angle remained unknown in each class. Multiple initial models were generated through random assignment of the remaining angle. The results were then refined using projection matching in IMAGIC and XMIPP (*15*). Additionally the entire dataset was analyzed using the 3-D maximum likelihood approach (*50*). In this case, the previously determined RCT model was low pass filtered to 50 Å and used as starting model. The resulting models (RCT, random assignment and maximum likelihood) provided a consensus agreement on the rise of the screw and all resulted in the characteristic oblique box-like feature along the filament.

To further limit the effect of heterogeneity in the RNP diameter and structure on the 3D map, straight filaments were carefully selected from the micrographs and extracted with 90% overlap using APPION (*52*). An adaptation of the iterative helical real space refinement (*53, 54*) was used to impose dihedral, helical symmetry on previously aligned particles. Initial helical parameters were estimated from analysis of non-symmetrized 2D class averages, as well as the models from the RNP segment analysis, without helical symmetry. Refinement was continued until the helical parameters were constant at 32.6 Å rise and 73.9˚ twist.

The RNP end regions were manually selected from the RNP cryo-EM images. The dataset was processed using the 3-D maximum likelihood approach as implemented in XMIPP. Five models were generated of which two were discarded after 50 iterations as they represented noise or poorly aligned particles. One of the other resulting classes showed a loop-like feature, whereas the remaining two represented a blunt end. The particles from the loop- and the blunt-end reconstructions were separated into individual datasets. In the case of the blunt-ends, particles belonging to either of the two reconstructions were merged. The two resulting datasets were then refined by 3-D maximum likelihood using three classes. The best models along with the respective single particles were then selected for each group, blunt- or loop-end, and refined using symmetry-free XMIPP projection matching.

For localization of the PB2 C terminus, RNPs containing PB2 C-terminal His_6-tag were gold labeled directly on the grid using Ni-NTA 5 nm Nanogold (Nanoprobes). After the RNP sample was applied to freshly glow-discharged, carbon-coated grids, the gold was directly applied and incubated for 30 min - 2 h in a humidity-saturated environment. After incubation, the

solution was blotted, stained, imaged and processed using similar protocols to the ones described above. The resulting stack was classified using 2-D maximum likelihood approaches (*16, 55*). This resulted in classes that contained gold bound to RNPs and gold that was randomly scattered over the grid, in which case no RNP was apparent in the class averages. All classes in which an RNP was not apparent were discarded leaving 32,407 particles in the stack. The pruned stack was then aligned against all results from the previous reference free run as a reference-based alignment (*56*).

To examine branched RNPs, we increased the dilution of the RNPs to minimize random overlaps so that each negatively stained micrograph contained only 1-3 full length RNPs. On average, one out of four RNPs was branched. Exemplar RNPs were manually selected and extracted from raw images.

Image analysis of free influenza virus polymerase

Initial models of the free influenza virus polymerase were created from data collected on negatively stained samples within IMAGIC using common lines on 2-D class-averages (*49*). Back projections of the resulting models were carefully compared against 2-D class-averages produced by reference free classification. The best model was low pass filtered to 50 Å and used as a starting model for 3-D maximum likelihood in XMIPP. The resulting three models showed good consensus at low resolution. The model that contained the largest number of particles was chosen as a starting model for 3-D refinement in XMIPP. The cryoEM dataset used for the analysis of the free polymerase was refined against the model that was previously calculated from negative stain data using the XMIPP projection matching protocol (*15*).

Docking of NP protomers into the central filament region

Automatic docking of individual NPs (PDB: 2IQH) into the central helical region volume was performed using the Chimera software package (*17*). In the first step, a single NP was positioned using the "fit in map search" function. 18 positions and orientations were automatically found, that included the entire model within the volume. The correlation coefficient of these different fits varied between 0.93 and 0.89 at 20 Å resolution. To generate the first of the two strands, the helical parameters were imposed on five additional copies of the NP structure. The result was duplicated yielding the second strand. The second strand was then manually orientated antiparallel into the EM-density. The position of both strands was then refined using the "fit in map" command. The resulting fit was then locally optimized using the "fit in map seq" function on all twelve individual NP structures respecting the helical symmetry. As a consequence of this optimization step, several docking solutions were identical and duplicates were discarded.

Two biological constraints were used to isolate the correct solution out of those remaining. First, on its putative pathway the RNA must enter and leave individual NPs at the same position without clashing into or wrapping around other NPs. Second, the position of the NLS-1 and 2 needed to correspond to the data described by Wu *et al.* (*18*), with NLS-1 being accessible from the outside and NLS-2 being buried within the helix. Only the docking solution presented meets all of these requirements.

Nascent RNP length measurements

Branched RNPs were identified in electron micrographs of a negatively stained sample prepared as described above. Measurements were made of the nascent RNP length, nascent RNP branch position and full-length RNP length. Because polymerase- and loop-ends are often

difficult to distinguish from one another, branch positions were measured as the distance from the nearest RNP filament end. Both nascent RNP length and branch position were normalized using the corresponding full-length RNP length. A total of 221 branched particles were analyzed (fig S15). For the plot in fig S15A a random jitter of up to 0.02 was applied to the data to spread overlapping data points. To determine the enrichment of particular nascent RNP lengths near the template RNP filament ends, branched RNPs were grouped by nascent RNP lengths. A nascent RNP was counted as being near the filament ends if the branch position was 10% or less of the template RNP length.

Influenza virus mini-genome assay

Mini-genome assays were performed as described (*57, 58*). Briefly, the *Gaussia* luciferase gene was cloned into pHW2000 that had been modified to omit the CMV promoter. Non-coding sequences of influenza A/Wilson-Smith/1933 (H1N1) virus gene segment 5, AGCAAAAGCAGGGTAGATAATCACTCACAGAGTGACATCGAAATC and AGAAAAATACCCTTGTTTCTACT (positive sense) were added at the 5′ and 3′ ends respectively of the *gluc* open reading frame. 23 ng of each DNA plasmid was transfected into a well of a 96-well plate with an 8:1 PEI Max:DNA (w/w) ratio. For the wild-type RNP transfection, cells received pHW191, pHW192, pHW193, pHW196, Gluc-pHW2000 (-CMV), and CMV-Cluc (New England Biolabs). For studying mutants, the appropriate plasmid was exchanged with a plasmid coding for the indicated mutation. 36 hours post-transfection, supernatants were diluted 1:20 into phosphate-buffered saline and 5 µL were used to separately assay for both *Gaussia* and *Cyprindina* luciferase activities on a Tecan Infinite F200Pro plate reader using a 50 µL auto-injection of the appropriate luciferase substrate, a 2 sec delay and 5 sec signal integration. All recorded signals were in the instrument's linear range. To correct for differences in transfection efficiency across the plate, *Gaussia* luciferase activity was calculated as the ratio of *Gaussia* luciferase activity to *Cyprindina* luciferase activity, the *Cyprindina* luciferase being expressed from a constitutive Pol II promoter. Experiments were normalized to the expression of *Gaussia* luciferase from a CMV promoter (CMV-Gluc, New England Biolabs) in a control sample (CMV).

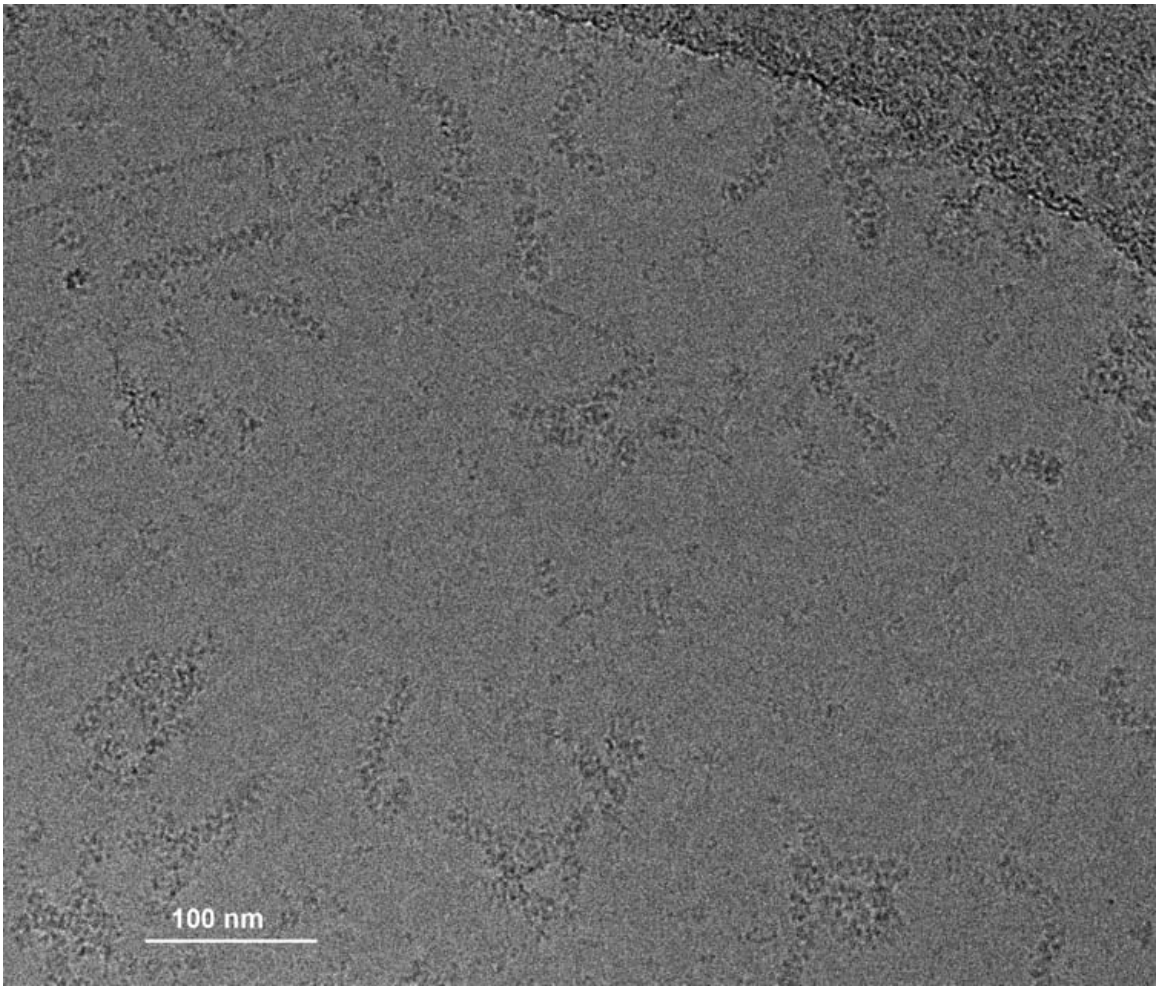

Fig. S1. Cryo-EM image of native influenza virus RNPs.

The large RNPs are approximately 110 nm long with a regular repeat and diameter though flexible along their length.

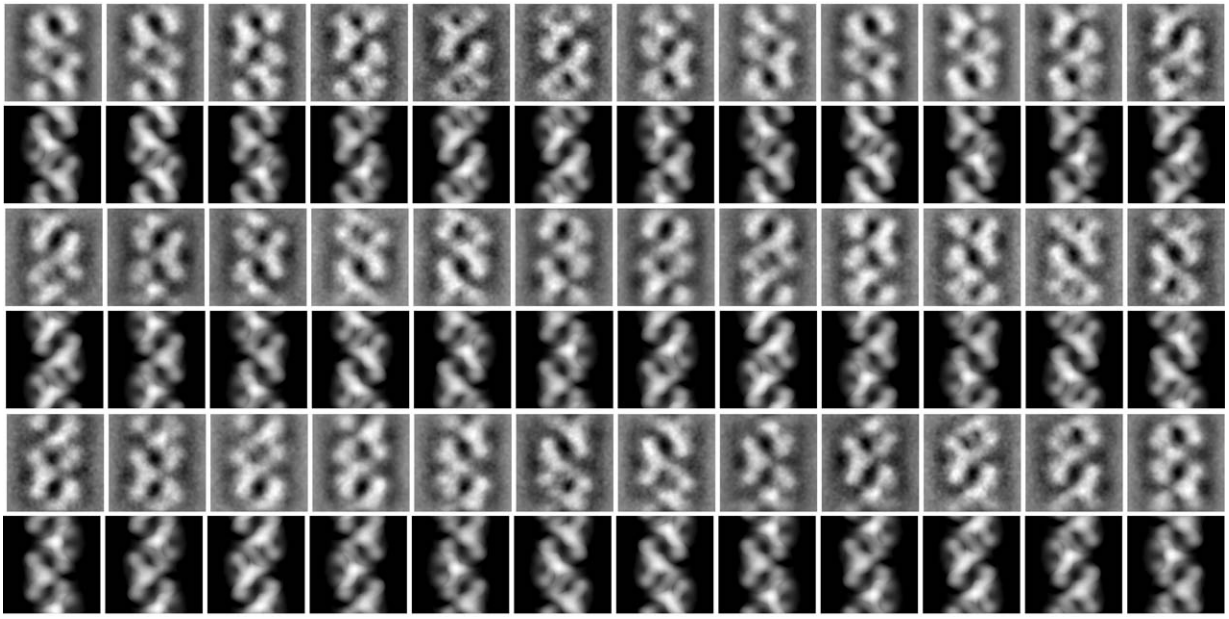

Fig. S2. 2-D class-averages and corresponding back-projections of the RNP filament.

Class-averages of the RNP filament (23 nm segment) reconstruction are shown in the upper row. The corresponding back-projections of the 21 Å 3-D reconstruction are shown at mass correlating threshold in the lower panel. Only in plane rotations of the volume are presented. The characteristic box-like feature along the length of the filament is clearly identifiable.

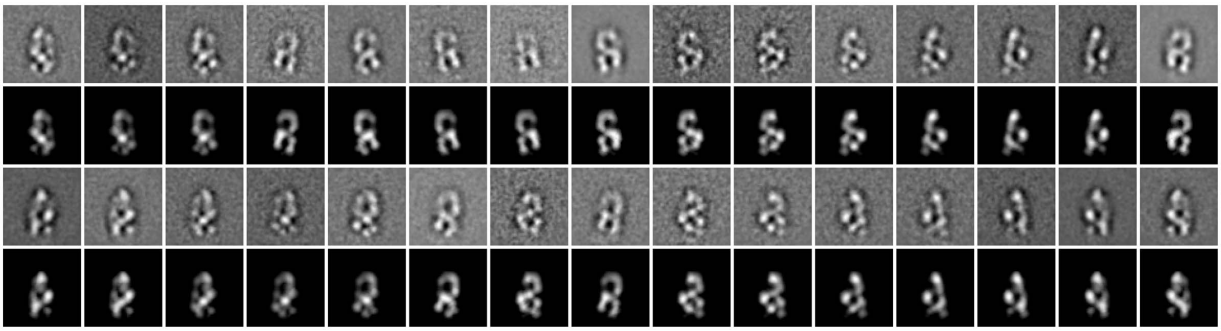

Fig. S3. 2-D class-averages and corresponding back-projections of the RNP looped-end.

Class averages are shown in the upper row and corresponding back projections are shown in the lower row. No out-of-tilt angles were taken into account for this representation. The resolution of the reconstruction is 40 Å.

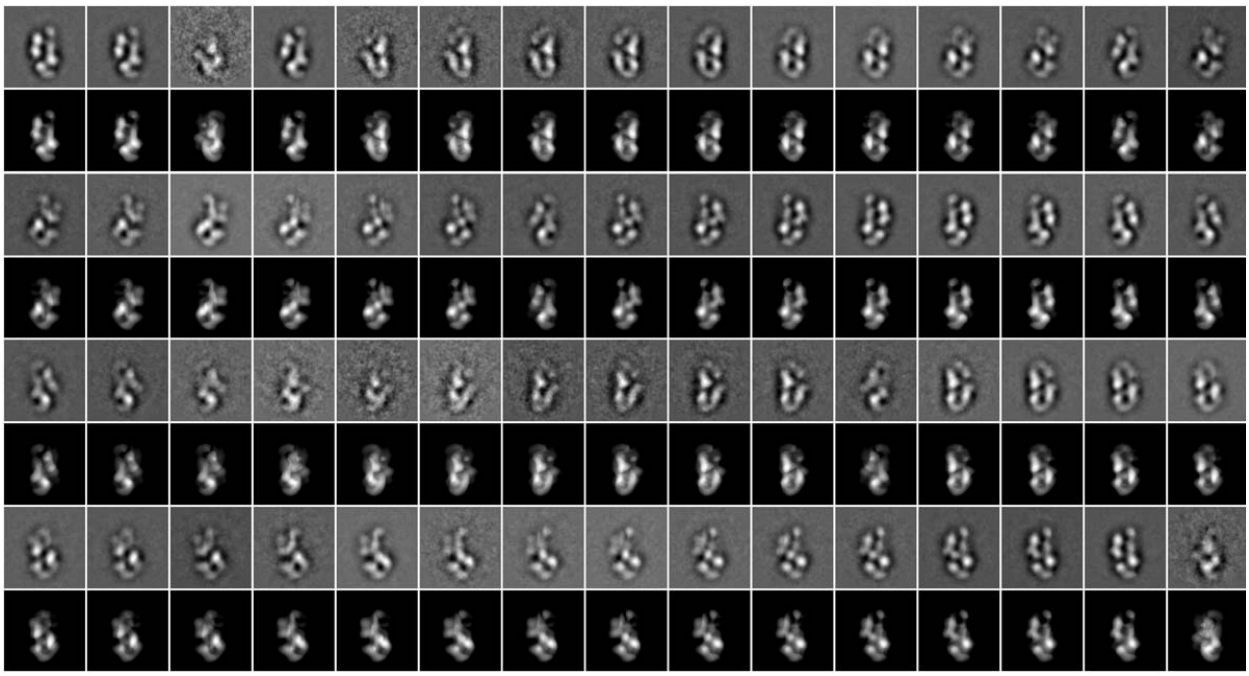

Fig. S4. 2D class-averages and corresponding back-projections of the polymerase-end.
Class-averages of the RNP polymerase-end dataset are shown in the upper row and the corresponding back-projections of the 3-D reconstruction at 20 Å, shown at mass correlating threshold, in the lower panel. Only in plane rotations of the volume are presented.

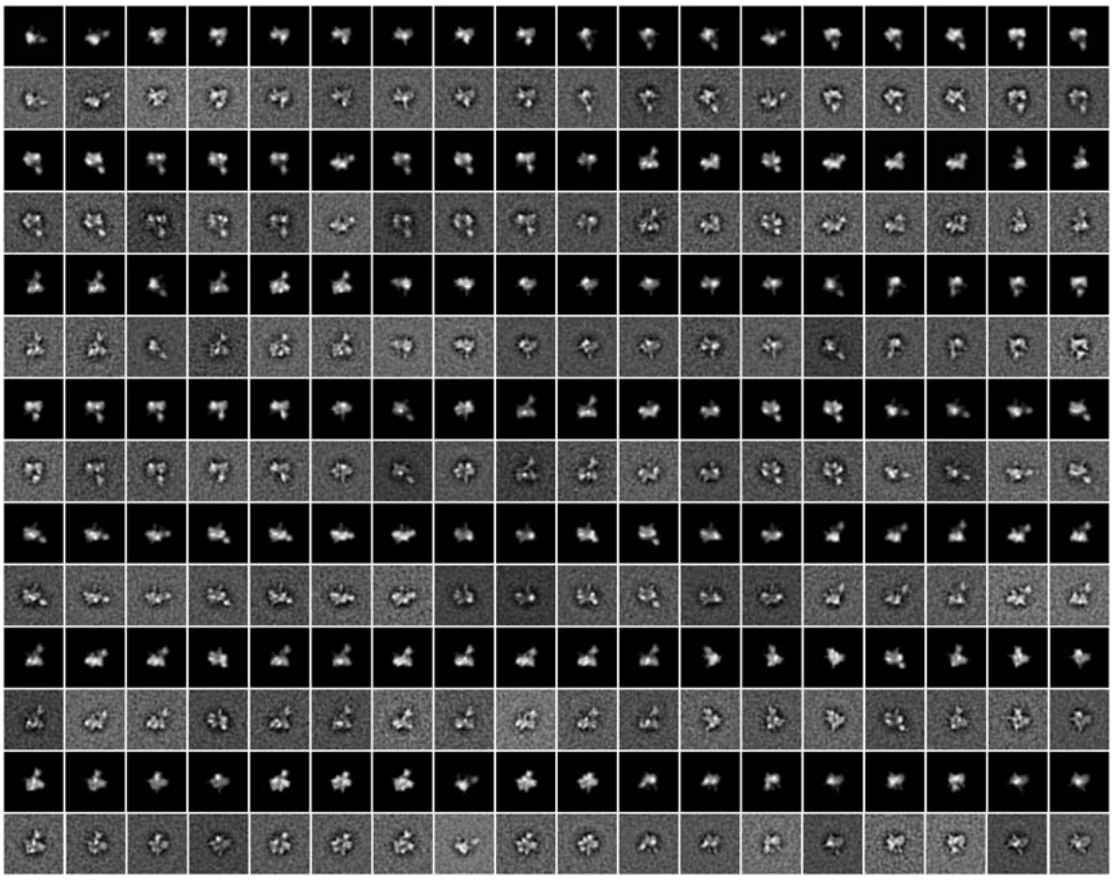

Fig. S5. 2-D class-averages and corresponding back-projections of the free RNA-polymerase.

Class-averages from cryo-EM of the free RNA-polymerase are shown in the upper rows. Back projections of the 3-D reconstruction are shown at mass correlating threshold (lower rows). The reconstruction is at 13 Å.

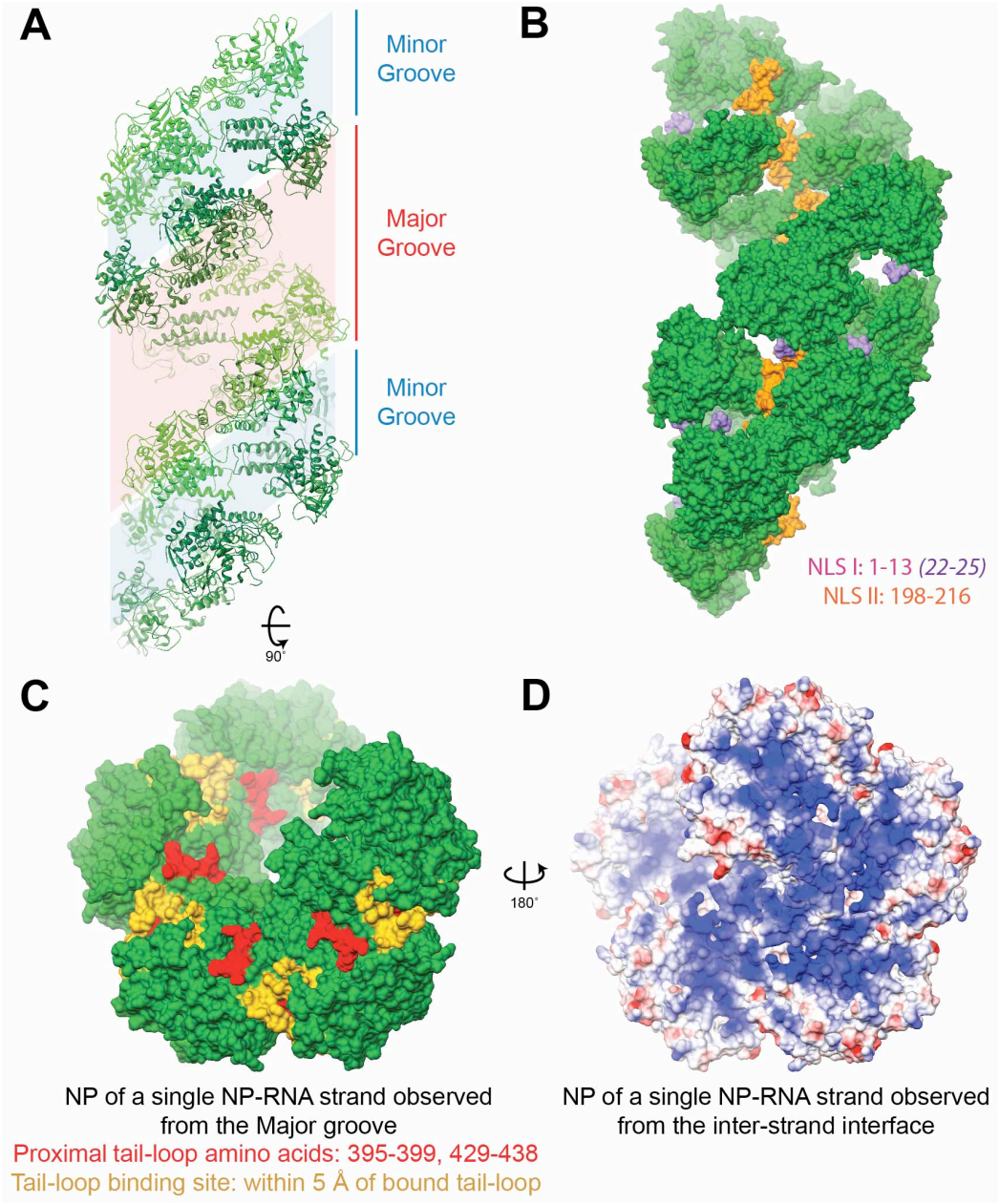

Fig. S6. Mapping of previous structural data onto the RNP central filament region.

The NP crystal structure (*9*) as docked into the cryo-EM reconstruction. (**A**) This panel denotes the major and minor grooves of the RNP central filament region. (**B**) The structures have been colored to highlight the exposure of NLS I between NP and the concealment of NLS II (orange) in the NP-NP interface. Amino acids 22-25 have been colored purple to mark the position of the N-terminal NLS I peptide disordered in the crystal structure. (**C**) Residues proximal to the NP tail-loop that are involved in oligomerization (red) or belonging to the tail-loop binding site (yellow) are situated along the major groove. (**D**) The NP composing a single strand of the double-stranded, anti-parallel RNP filament as viewed from within the minor groove and shown below as a Coulombic surface (+/- 10 kcal/(mol•e)) to highlight the electropositive RNA binding sites buried in the NP-NP inter-strand interface.

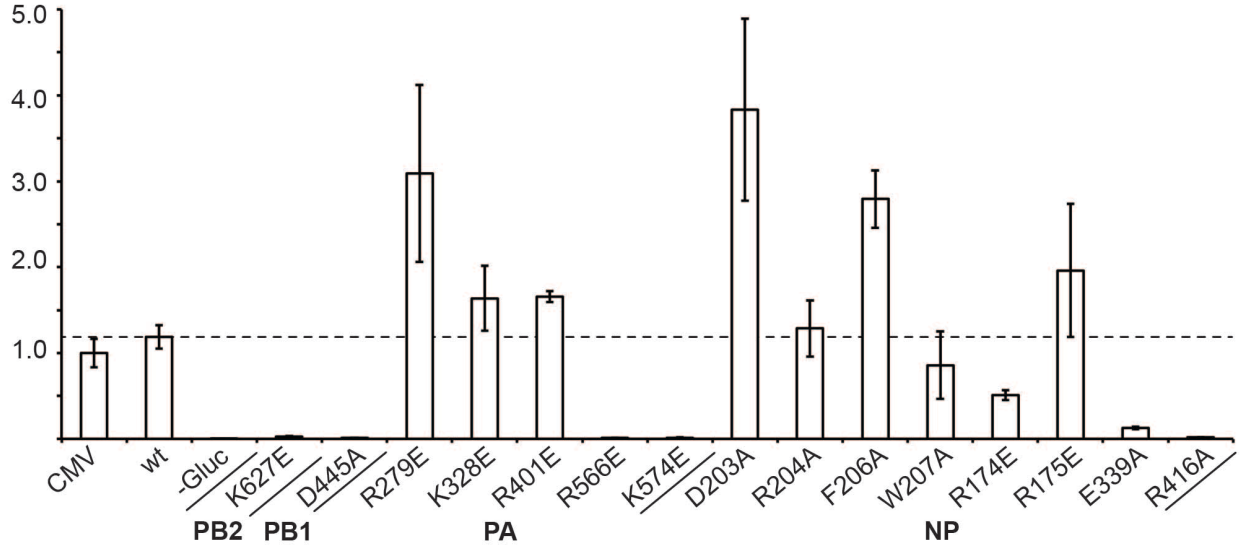

Fig. S7. Influenza virus mini-genome assay.

Expression of *Gaussia* luciferase reports on the functionality of mutants of the RNP components. The ordinate values represent the normalized average *Gaussia* luciferase activity with error bars representing the standard deviation of three experiments. CMV represents the luciferase expressed from a constitutive promoter; in all other cases presented, the RNP transcribes the *Gaussia* luciferase. The -Gluc value is from a sample transfected with all RNP components and excluding the reporter plasmid. The dashed line indicates the wild-type level of RNP transcriptional activity.

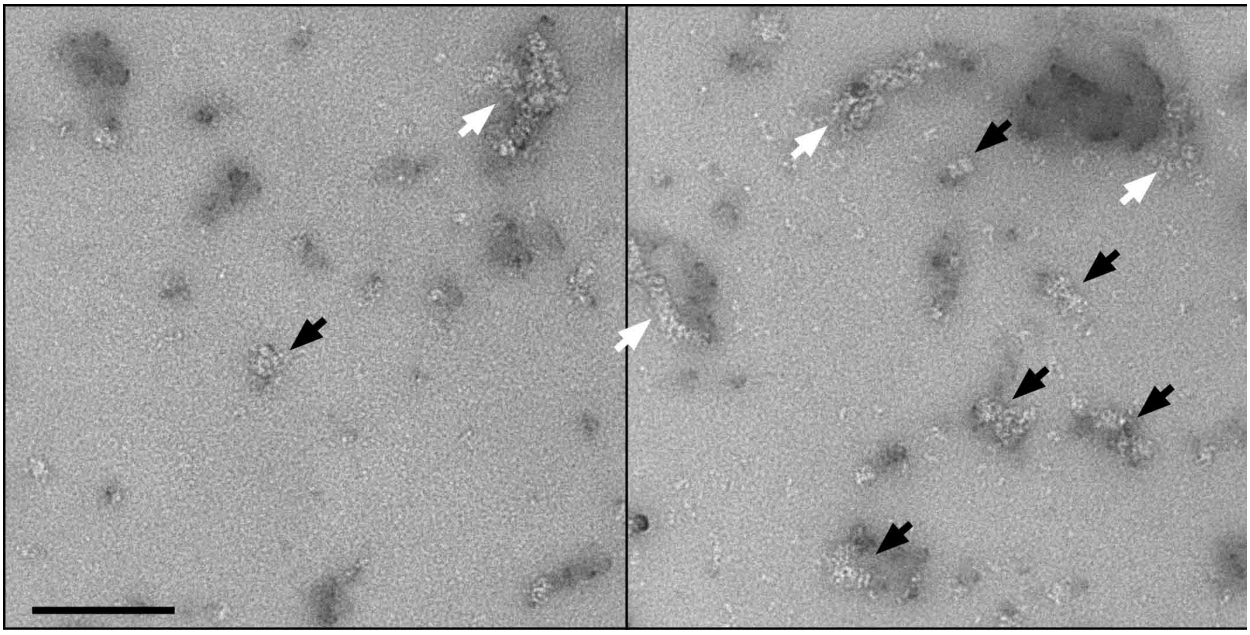

Fig. S8. Mutant RNPs fail to assemble properly.

These two micrographs show the effect of D203A mutation of the NP head domain on RNP formation using negative stain EM. While some RNPs still assemble (white arrows) into a helical filament, their overall count is significantly reduced compared to the usual preparation. A large number of aggregated NPs can be found in the background (black arrows), which is a possible explanation for the reduced number. Scale bar corresponds to 50 nm.

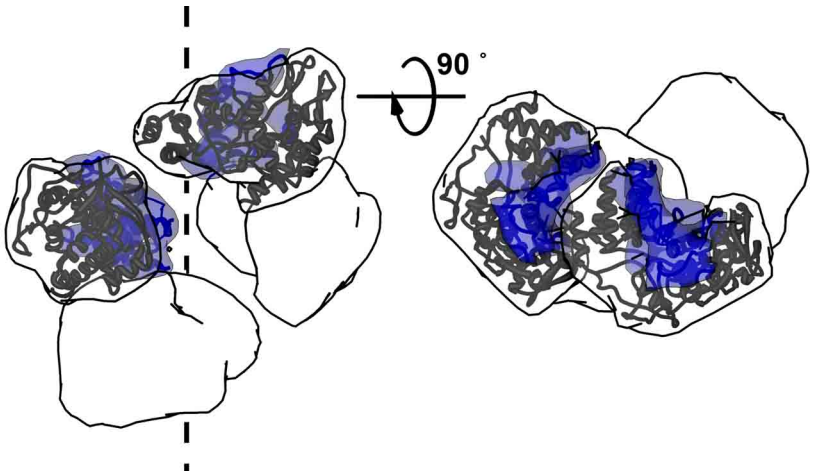

Fig. S9. Fitted NP protomers leave gaps between consecutive NPs.

NP protomers fit into the helical reconstruction of the central filament region have periodic gaps between them. The putative RNA binding site is colored in blue. The dashed line represents the RNP filament helical axis.

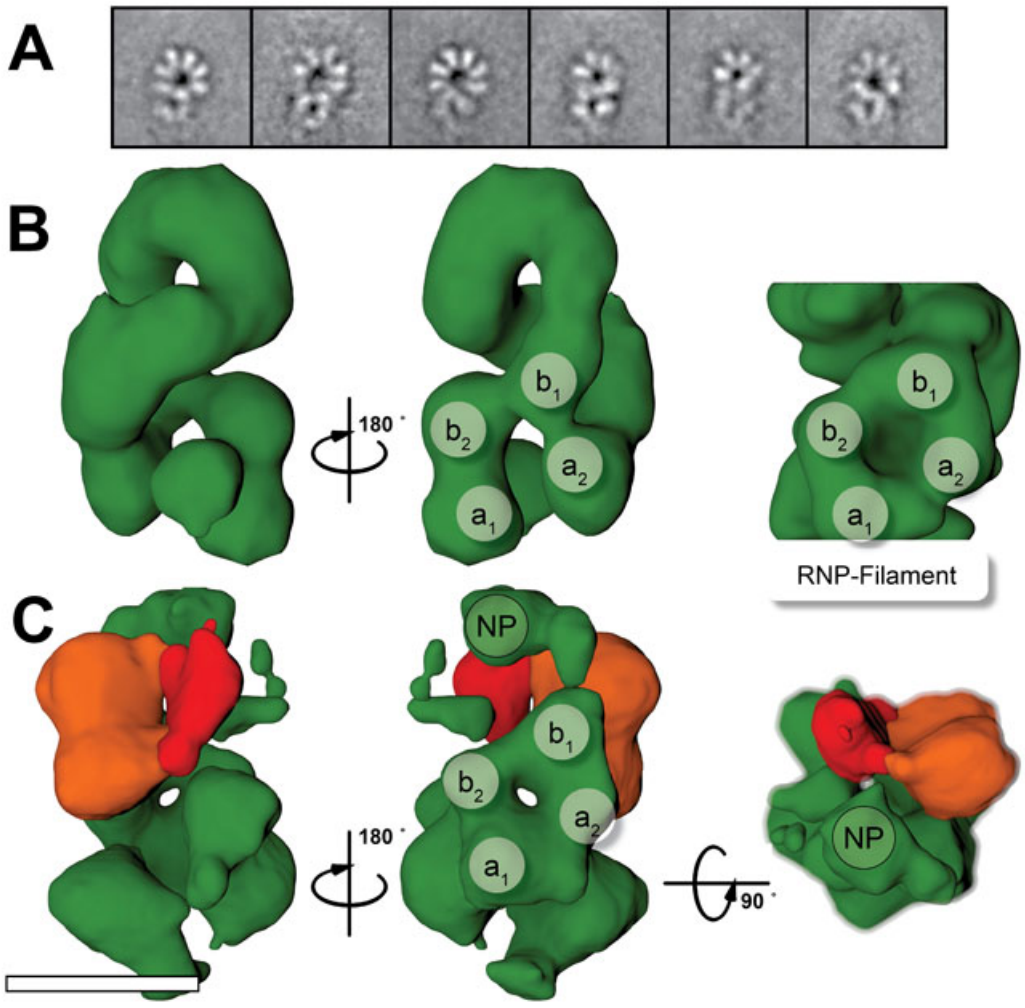

Fig. S10. RNP end-regions.

(A) 2-D class averages of the loop region calculated from images of negatively stained samples. Different numbers of NPs (5-8) result in a variation of loop diameter. **(B)** Cryo-EM reconstruction of a narrow looped-end. The path of the loop most closely corresponds to a loop of five NPs seen in (A). The reconstructed volume also contains a short region from the central filament. The characteristic box-like feature formed from four NPs in the loop region is numbered and shown next to an equivalent section from the main RNP-filament region for comparison. (**C**) Cryo-EM reconstruction of the RNA polymerase end (polymerase large and arm domains colored red and orange respectively and nucleoprotein colored green). NPs belonging to the characteristic box-region as well as an additional NP not part of the helical filament are labeled. Scale bar represents 10 nm.

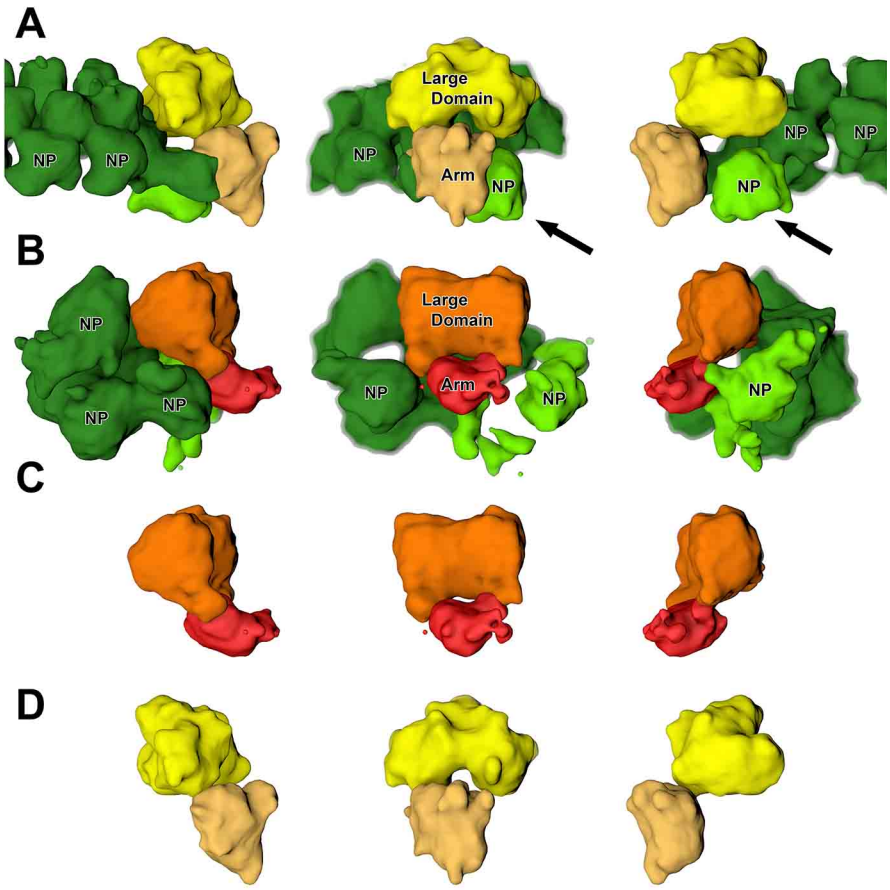

Fig. S11. Comparison of native influenza virus RNP with mini-RNP.

(**A**) Previous reconstruction shown with NP in dark green, polymerase large domain in yellow, polymerase arm domain in gold. An additional density previously thought to be part of polymerase is here denoted as NP colored in light green and indicated with an arrow. (**B**) Corresponding views of the native RNP-bound polymerase presented in this study. (**C** and **D**) Polymerase structures isolated from NP components corresponding to the views in B and A respectively. The previously published reconstruction is scaled at 2.4 $Å^3$/voxel.

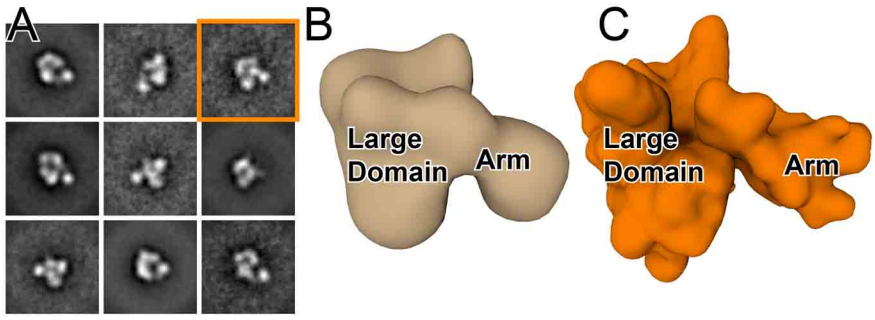

Fig. S12. Reconstruction of the influenza virus RNA-polymerase.

(**A**) Similar to the Machupo virus polymerase (*29*), 2-D class-averages of the negatively stained influenza virus polymerase shows a large domain and an arm domain. (**B**) 3-D surface representation of the reconstruction from negatively stained influenza virus RNA-polymerase at 23 Å resolution and (**C**) the corresponding representation from cryo-EM at 13 Å resolution. The upper right class-average in A corresponds to the views of polymerase in B and C.

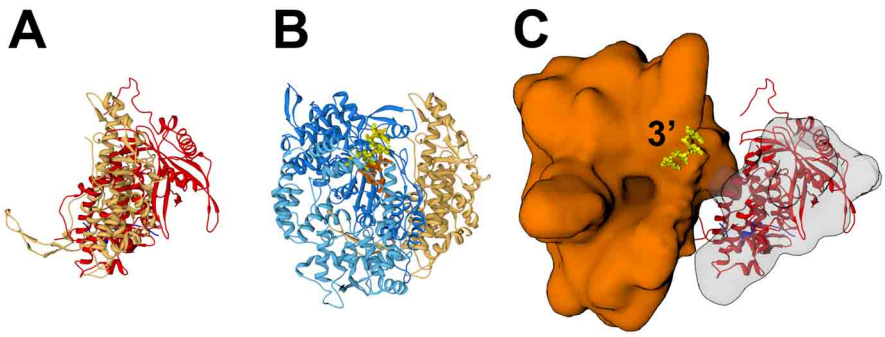

Fig. S13. Structural homology of influenza virus polymerase with reovirus λ3.

(**A**) Superimposition of the influenza virus PA CTD with the λ3 RNA polymerase N-terminal domain showing structural homology between the two domains(*30*). (**B**) Corresponding view of the complete reovirus polymerase with bound template (yellow) and complementary dideoxy-nucleotide triphosphates (orange). (**C**) The 3′ RNA template transferred onto the influenza virus polymerase based on the structural homology in A.

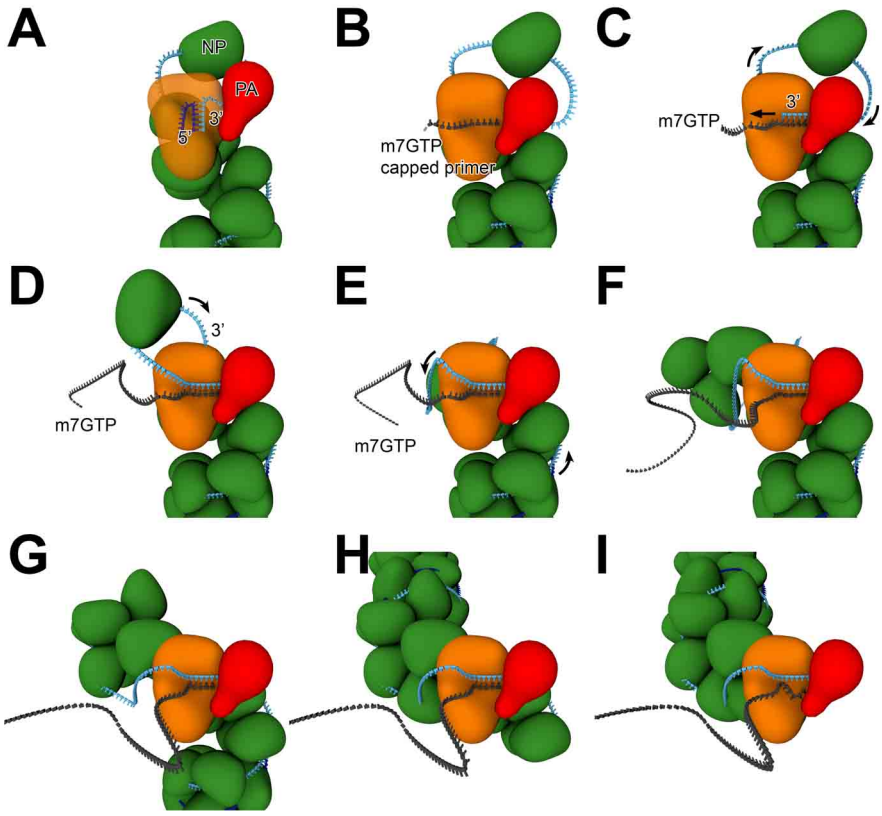

Fig S14. Model for influenza virus transcription.

Transcription is carried out by the resident polymerase component of the RNP complex. The polymerase large and arm domains are shown in orange and red respectively. Nucleoprotein is colored green, template RNA is shown in blue and product mRNA is colored black. (**A**) The process is initiated by binding both of the 5′ and 3′ template termini leading to (**B**) binding and cleavage of capped oligonucleotides used to initiate transcription. (**C**) The 3′ end disengages from the 5′ end and repositions into the polymerase active site. (**D**) As the polymerase elongates the transcript, the 3′ end rebinds the polymerase and re-encapsidates the template with NP. (**E-H**) As the transcript is elongated, the transcribed template RNA-NP complex coils up into a RNP-like structure producing a kink in the RNP. (**I**) Throughout transcription, polymerase remains bound to the 5′ terminus of the genome. As the transcribing polymerase nears the 5′ end of the template, it pulls a polyuridine stretch across the active site. The polymerase is unable to transcribe further along the template and stutters across these uridine residues, polyadenylating the viral mRNA and terminating transcription. The RNP may undergo transient unwinding throughout this process to facilitate the movement of NPs.

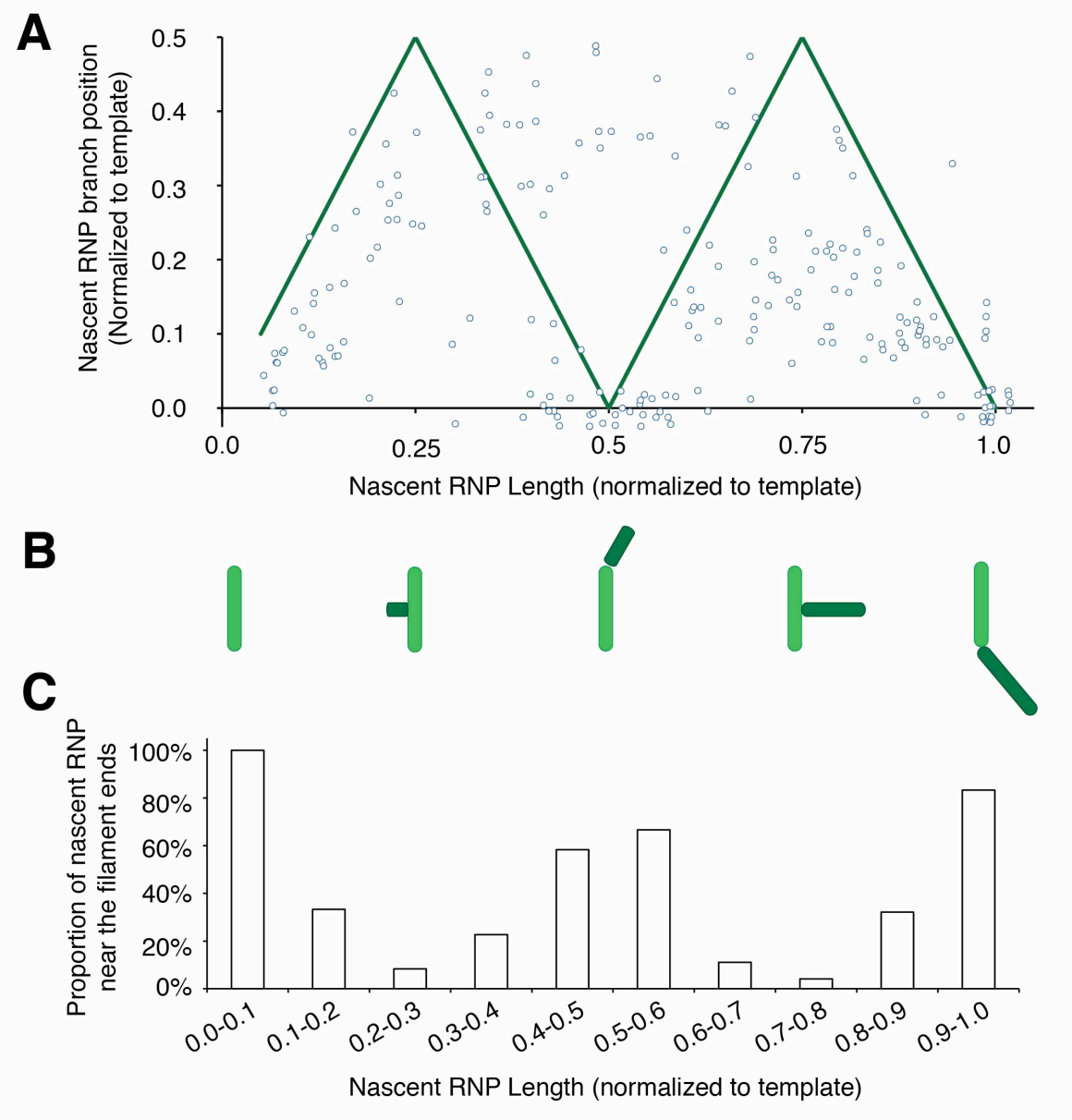

Fig. S15. Correlating the length of nascent RNPs to template branch position.

(**A**) The nascent RNP branch position is plotted against the length of the nascent RNP. Both nascent RNP position and length are reported as a fraction of the full-length RNP. Because RNP filament ends are not easily distinguished from one another, branch position is reported as the relative distance to the nearest end and is on a scale of 0-0.5. Data points are shown as circles and the idealized pattern of nascent RNP lengths and branch positions is shown as a solid green line. A random jitter of up to 0.02 was applied to better spread overlapping points. (**B**) Cartoon representations of RNP replication intermediates with the length of the nascent RNP (dark green) varying with branching position on the template RNP (light green). (**C**) The data from **A** presented to show that certain RNP lengths are greater populated near the filament ends. Branch positions within 10% of the template RNP length from the filament ends were used for this representation.

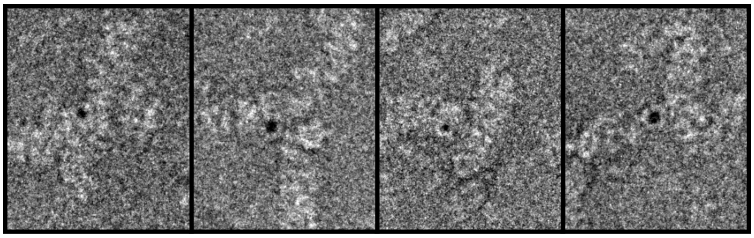

Fig. S16. Gold labeling of branched RNPs.

PB2 was C-terminally His_6-tagged and RNP filaments were labeled with Ni-NTA 5 nm Nanogold. Images identify the polymerase at the RNP branch junctions.

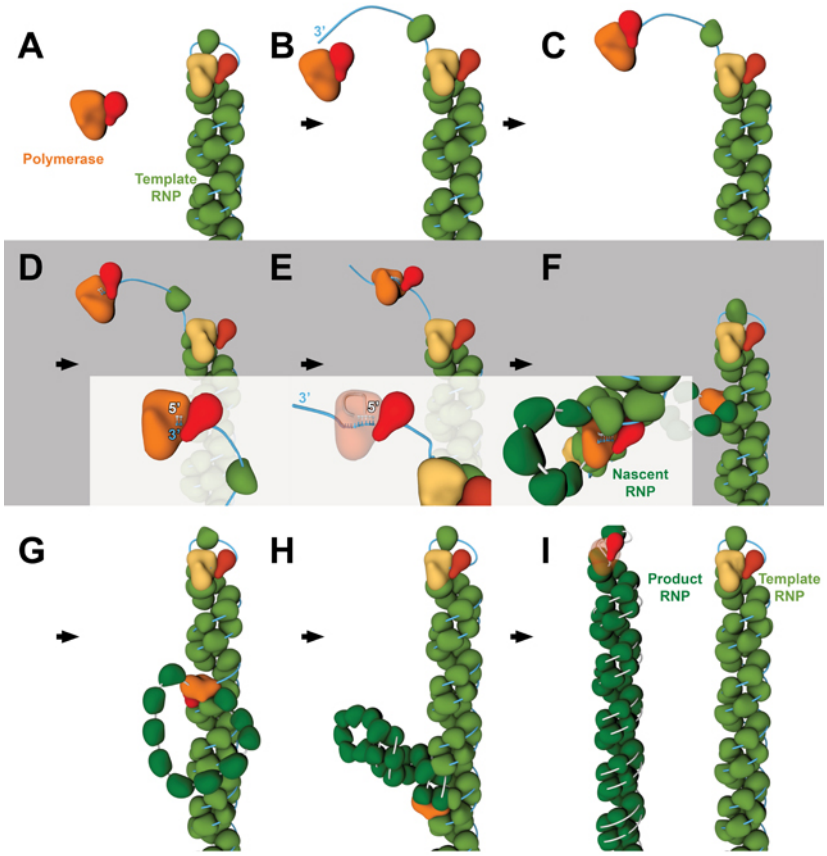

Fig. S17. Model for influenza virus replication.

(**A**) Replication of the viral genome is carried out by a second polymerase acting on an RNP template *in trans*. The polymerase large and arm domains are in orange and red respectively. On the template RNP, RNA is colored blue and NP in light green. On the nascent/product RNP, RNA is colored white and NP in dark green. (**B**) The 3′ end of the template RNA disengages from the 5′ end and (**C**) finds its way into the active site of the second polymerase. (**D**) RNA synthesis during replication is initiated *de novo* by the synthesis of a pppApG dinucleotide. (**E**) As the replicating polymerase elongates along the template, a new 5′ terminus is produced which is bound by the replicating polymerase. (**F**) This also initiates encapsidation of the product RNA by NP in a 5′ to 3′ direction forming a nascent RNP complex. In order to gain access to the template RNA, the NPs are removed from the template RNP and then returned after RNA synthesis. (**G**) Upon reaching a length of approximately twelve NP, the looped NP-RNA strand coils into a helical filament (**H**). (**I**) The nascent RNP continues elongating along the template RNP, terminating replication at the 5′ end of the template to produce a fully assembled RNP complex. Proposed intermediates from steps F-H during the elongation phase give the RNP a branched appearance in electron micrographs. The RNP may undergo transient unwinding throughout this process to facilitate the movement of NPs and produce the filament structures observed in Fig. 4.

Particle Examined	Nominal Magnification	Pixel-size [Å]	Dose [e-/Å]	Micrographs	Particles	Particle Selection	Box Size	Binning Factor	Underfocus [µm]	Resolution [Å]
RNP helical segment *cryo*	50,000	1.64	15	3,437	289,617	template	200,200	4	1.5,3.1	
RNP helical segment *cryo*	50,000	1.64	15	3,437	31,573	manual, 90% overlap	144,144	1	1.5,3.0	21
RNP polymerase end *cryo*	50,000	1.64	15	3,437	55,013/8,484	manual	200,200	1	1.5,3.1	20
RNP looped end *cryo*	50,000	1.64	15	3,437	55,013/5,549	manual	200,200	4	1.5,3.2	~40
RNP *stain*	50,000	1.64	45	108	3,672	manual	64,64	2	1.0,2.0	
RNP branches *stain*	50,000	3.28	45	2,661		manual			3.0	
Polymerase *cryo*	100,000	1.09	20	1,878	16,958	DoG-Picker	128,128	1	1.5,4.0	13
Polymerase *stain*	50,000	2.18	45	875	100,000	DoG-Picker	64,64	2	0.5,1.3	~23
Polymerase AU *stain*	50,000	1.64	20	2,058	93,007	DoG-Picker	512,512	2	1.0,2.0	

Table S1. Summary of electron microscopy experiments.

Particles are grouped by shading according to specimen. The two sets of particles for RNP helical segment cryo-EM were selected using different methods. The exact values used in the reconstruction of the RNP filament with helical symmetry are 32.59217 Å rise and 73.92063˚ twist. Although these values are not accurate to this many significant figures, these are the values used for helical fitting of NP monomer structures into the reconstruction. The number of particles used for reconstruction of the RNP polymerase and looped ends is presented as the total number of particles in the final stack followed by the number of particles used for the reconstruction. For the RNP branches examined in stain, images were extracted from raw micrographs and were not CTF-corrected; hence, a single underfocus value is reported. Resolutions are reported for those data for which a 3-D reconstruction is calculated and represent the resolution of the data at a Fourier Shell Coefficient of 0.5.

Movie S1. Central filament region. The NP crystal structure is docked into the central filament region reconstruction. NPs belonging to antiparallel strands are colored light and dark blue. The NPs were positioned into the 20 Å reconstruction using automated docking procedures and imposing helical and dihedral symmetry.

Movie S2. Model for influenza virus transcription. This animation depicts the transcription steps outlined in fig. S10. Transcription is carried out by the resident polymerase component of the RNP complex. The polymerase large and arm domains are shown in orange and red respectively. Nucleoprotein is colored green, template RNA is shown in blue, and product mRNA is colored white. Transcription is initiated with both of the 5′ and 3′ template termini bound, leading to the generation of a capped oligonucleotide used to prime transcription. The 3′end (light blue) disengages from the 5′end and repositions into the polymerase active site. As the polymerase elongates the transcript, the 3′end rebinds the polymerase and re-encapsidates the template with NP. As the transcript is elongated, the transcribed template RNA-NP complex coils up into a RNP-like structure producing a kink in the RNP. Throughout transcription, polymerase remains bound to the 5′ terminus of the genome. As the transcribing polymerase nears the 5′ end of the template, it pulls a polyuridine stretch across the active site. The polymerase is unable to transcribe further along the template and stutters across these uridine residues, polyadenylating the viral mRNA and terminating transcription. The RNP may undergo transient unwinding throughout this process to facilitate the movement of NPs; however, NPs are shown to slide past on another in this representation to simplify the model.

Movie S3. Model for influenza virus replication. This animation depicts the replication steps outlined in fig. S12. A second polymerase acting on an RNP template carries out replication of the viral genome. The polymerase large and arm domains are in orange and red respectively. On the template RNP, RNA is colored blue and NP in light green. On the nascent/product RNP, RNA is colored white and NP in dark green. The 3′ end of the template RNA disengages from the 5′end and finds its way into the active site of the second polymerase. As the replicating polymerase elongates along the template, a new 5′ terminus is produced and is bound by the replicating polymerase. This binding initiates encapsidation of the product RNA by NP in a 5′ to 3′ direction forming a nascent RNP complex. In order to gain access to the template RNA, the NPs are removed from the template RNP and then returned after RNA synthesis. Upon reaching a length of approximately twelve NP, the looped NP-RNA strand coils into a helical filament. Proposed intermediates during the elongation phase give the RNP a branched appearance in electron micrographs. The nascent RNP continues elongating along the template RNP, terminating replication at the 5′ end of the template to produce a fully assembled RNP complex. The RNP may undergo transient unwinding throughout this process to facilitate the movement of NPs and produce the filament structures observed in Fig. 4.